Radiation Dosimetry and Biodistribution of ^{68}Ga-FAPI-46 PET Imaging in Cancer Patients

Catherine Meyer[1,2], Magnus Dahlbom[1,2], Thomas Lindner[3], Sebastien Vauclin[4], Christine Mona[2], Roger Slavik[1,2,5], Johannes Czernin[2,6,7], Uwe Haberkorn[3,7,8], and Jeremie Calais[1,2,5,6]

[1]Physics and Biology in Medicine Interdepartmental Graduate Program, David Geffen School of Medicine, UCLA, Los Angeles, California; [2]Ahmanson Translational Theranostics Division, Department of Molecular and Medical Pharmacology, UCLA, Los Angeles, California; [3]Department of Nuclear Medicine, University Hospital Heidelberg, Heidelberg, Germany; [4]DOSIsoft SA, Cachan, France; [5]Jonsson Comprehensive Cancer Center, UCLA, Los Angeles, California; [6]Institute of Urologic Oncology, UCLA, Los Angeles, California; [7]Clinical Cooperation Unit Nuclear Medicine, DKFZ Heidelberg, Heidelberg, Germany; and [8]Translational Lung Research Center Heidelberg, German Center for Lung Research, Heidelberg, Germany

Targeting cancer-associated fibroblasts (CAFs) has become an attractive goal for diagnostic imaging and therapy because they can constitute as much as 90% of a tumor mass. The serine protease fibroblast activation protein (FAP) is overexpressed selectively in CAFs, drawing interest in FAP as a stromal target. The quinoline-based FAP inhibitor (FAPI) PET tracer ^{68}Ga-FAPI-04 has been previously shown to yield high tumor-to-background ratios (TBRs) in patients with various cancers. Recent developments toward an improved compound for therapeutic application have identified FAPI-46 as a promising agent because of an increased tumor retention time in comparison with FAPI-04. Here, we present a PET biodistribution and radiation dosimetry study of ^{68}Ga-FAPI-46 in cancer patients. **Methods:** Six patients with different cancers underwent serial ^{68}Ga-FAPI-46 PET/CT scans at 3 time points after radiotracer injection: 10 min, 1 h, and 3 h. The source organs consisted of the kidneys, bladder, liver, heart, spleen, bone marrow, uterus, and remainder of body. OLINDA/EXM software, version 1.1, was used to fit and integrate the kinetic organ activity data to yield total-body and organ time-integrated activity coefficients and residence times and, finally, organ-absorbed doses. SUVs and TBR were generated from the contoured tumor and source-organ volumes. Spheric volumes in muscle and blood pool were also obtained for TBR (tumor SUV_{max}/organ SUV_{mean}). **Results:** At all time points, average SUV_{max} was highest in the liver. Tumor and organ SUV_{mean} decreased over time, whereas TBRs in all organs but the uterus increased. The organs with the highest effective doses were bladder wall (2.41E−03 mSv/MBq), followed by ovaries (1.15E−03 mSv/MBq) and red marrow (8.49E−04 mSv/MBq). The average effective total-body dose was 7.80E−03 mSv/MBq. **Conclusion:** ^{68}Ga-FAPI-46 PET/CT has a favorable dosimetry profile, with an estimated whole-body dose of 5.3 mSv for an administration of 200 MBq (5.4 mCi) of ^{68}Ga-FAPI-46 (1.56 ± 0.26 mSv from the PET tracer and 3.7 mSv from 1 low-dose CT scan). The biodistribution study showed high TBRs increasing over time, suggesting high diagnostic performance and favorable tracer kinetics for potential therapeutic applications.

Targeting the stroma in the tumor microenvironment has become an attractive goal for diagnostic imaging and therapy (1–3). Cancer-associated fibroblasts (CAFs) are the predominant component of the stroma surrounding epithelial cancer cells, and they can compose up to 90% of the total tumor mass in desmoplastic cancers (4–7). These reactive stromal cells selectively produce fibroblast activation protein (FAP), a serine protease that is scarcely expressed within the stroma of healthy tissues (1,4,5). FAP-positive CAFs are reported to promote and enhance protumorigenic characteristics such as angiogenesis, neoplastic progression, metastatic invasion, and migration (4,8–14). FAP expression is high in CAFs but low in normal adult tissues, except for sites of active tissue damage, remodeling, and inflammation (4).

The specificity of FAP for CAFs in the tumor microenvironment provided the motivation to develop FAP-specific small-molecule inhibitors. Several quinoline-based FAP inhibitors (FAPIs) labeled with positron emitters have been developed (15–17). FAPI-04 labeled with ^{68}Ga provided PET images with high tumor-to-background ratios (TBRs) in patients across a wide array of cancers, suggesting high potential for FAP-targeted diagnostics and possibly molecular radiotherapy (17–20). Because the stroma can represent up to 90% of the total tumor mass, stroma-targeted PET imaging may be more sensitive than glucose metabolism PET imaging for tumor detection in some cancers (16,18,21,22). In the context of stroma-targeted radionuclide therapy, breaking the tumor stroma barrier may increase tumor cell accessibility for pharmacologic, immunologic, or cell-based therapies (10–12). Additionally, delivery of ionizing radiation to the cancer cells may also be possible by crossfire effect.

In an effort to increase FAPI tumor uptake and retention for therapeutic applications, related FAPI-04 derivatives were developed and assessed preclinically and in cancer patients (17). From these studies, FAPI-46 emerged as the most promising tracer for therapeutic clinical application because of its high tumor uptake and retention and its decreased uptake in normal organs compared with FAPI-04.

As a required step for further translation and approval by regulatory agencies, the primary objective of this study was to provide the radiation dosimetry analysis in cancer patients who underwent ^{68}Ga-FAPI-46 PET imaging. The secondary aim was to describe the organ biodistribution, SUV metrics, and temporal changes in TBRs (tumor SUV_{max}/organ SUV_{mean}).

MATERIALS AND METHODS

Study Design and Patients

This was a retrospective study of radiation dosimetry and biodistribution of a novel PET imaging probe. The imaging data were acquired at the Heidelberg University Hospital in Germany. The analysis was conducted at UCLA. Six patients (4 men, 2 women; age range, 56–81 y) with different cancer types were included. All 6 patients were referred for an unmet diagnostic challenge that could not be solved sufficiently with standard diagnostic imaging. The patient characteristics are summarized in Table 1. All patients gave written informed consent to undergo FAPI PET/CT. Following the regulations of the German Pharmaceuticals Act §13(2b), indication and labeling of the FAPI tracers were under the direct responsibility of the applying physician. The data were analyzed retrospectively with the approval of the local ethics committee (approval S016/2018).

Radiopharmaceutical Synthesis

The radiotracer synthesis was conducted as previously described (15–17). Briefly, radiolabeling was performed by adjusting a mixture of 20 nmol of FAPI-46, 10 μL of ascorbic acid solution (20% in water), and 1 mL of ^{68}Ga-solution (0.6–2 GBq in 0.6 M HCl in water) to pH 3.3–3.6 with sodium acetate (2.5 M in water). After being heated to 95°C for 20 min, the product was isolated by solid-phase extraction (Oasis Light HLB; Waters) using 0.5 mL of ethanol as the eluent. After dilution with 5 mL of sodium chloride solution (0.9%), the pH was adjusted to 7 by the addition of phosphate buffer.

PET/CT Image Acquisition

Injected activity was limited to 100–370 MBq per examination based on previous dosimetry estimates of related FAPIs with an effective whole-body dose of 1.6 mSv/100 MBq as well as count rate considerations (21). Each patient underwent PET/CT imaging scans at 3 time points after radiotracer injection: 10 min (before voiding), 1 h, and 3 h. No bladder voiding model was used, and thereby the calculated bladder dose will be the maximum dose assuming no voiding. All imaging was performed on a Biograph mCT Flow scanner (Siemens). After non–contrast-enhanced low-dose CT had been performed (130 keV, 30 mAs, CareDose; reconstructed with a soft-tissue kernel to a slice thickness of 5 mm, increment of 3–4 mm), PET images were acquired in 3-dimensional mode (matrix, 200 × 200) using FlowMotion (Siemens) with 0.7 cm/min continuous bed motion. The emission

data were corrected for randoms, scatter, and decay. Reconstruction was performed using ordered-subset expectation maximization with 2 iterations and 21 subsets and Gauss-filtering to a transaxial resolution of 5 mm in full width at half maximum. Attenuation correction was performed using the nonenhanced low-dose CT data.

Radiation Dosimetry

Mean absorbed radiation doses were estimated using the source and target organ framework outlined by the MIRD Committee (23,24). Organ delineation and activity accumulation at each imaging time point was determined using PLANET Dose internal dosimetry software (DOSIsoft SA). Time–activity curve fitting and subsequent dose calculation was performed using OLINDA/EXM, version 1.1. The source organs consisted of the kidney parenchyma, urinary bladder, liver, heart contents, spleen, bone marrow, uterus, and remainder of body. Source organs were chosen on the basis of highest tracer uptake and previously published work (21).

Source organ volumes of interest were contoured manually at the first time point and propagated to later-time-point scans on the basis of automatic deformable registration between each scan. Propagated organ volumes were then manually adjusted when necessary. Organ volume differences that arose because of elastic propagation between time points were accounted for by calculating the mean volume for organ mass input for dose calculation in OLINDA/EXM. Kidney volumes included left and right renal parenchyma, excluding the urinary activity in renal calyces, as shown in Figure 1. The urinary activity (Fig. 1B) was delineated using SUV thresholding and subsequently subtracted from the entire kidney volume to yield only kidney parenchyma (Fig. 1C). Activity in the bone marrow was determined by contouring 2 lumbar vertebrae and scaling on the basis of the proportion of total-body bone marrow mass, with each vertebra assumed to contain 2.5% (25).

In all cases, tumor lesion activity was excluded from normal-organ source volumes by Boolean subtraction operations and incorporated in the body remainder term. Tumors were contoured using patient-specific SUV thresholding with manual adjustment (SUV threshold ranged from 2.5 to 3.5). The body remainder volume was determined by subtracting all source organs from a whole-body contour.

After tumor and organ contouring, the non–decay-corrected percentage injected activity accumulated in the organs at each time point per patient was then used as input for OLINDA/EXM software.
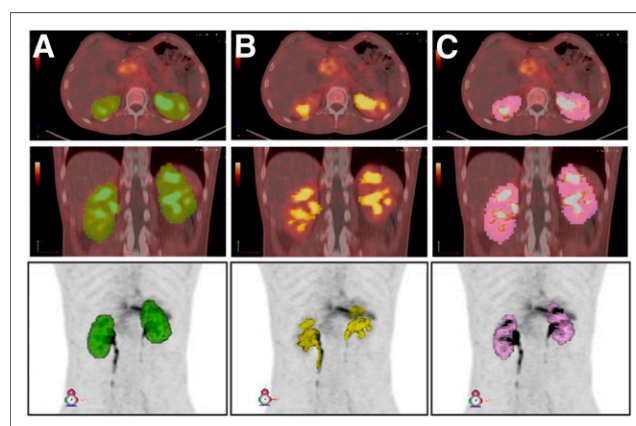

FIGURE 1. Delineated volumes used for determination of renal cortex volume: entire kidney volume (A) from which urine, including in renal calyces, is subtracted (B) to yield renal cortex volume (C). Images are shown for patient 6 and are representative of method applied for all patients. All volumes are shown in axial (top), coronal (middle), and maximum-intensity-projection views (bottom).

TABLE 1
Patient Characteristics

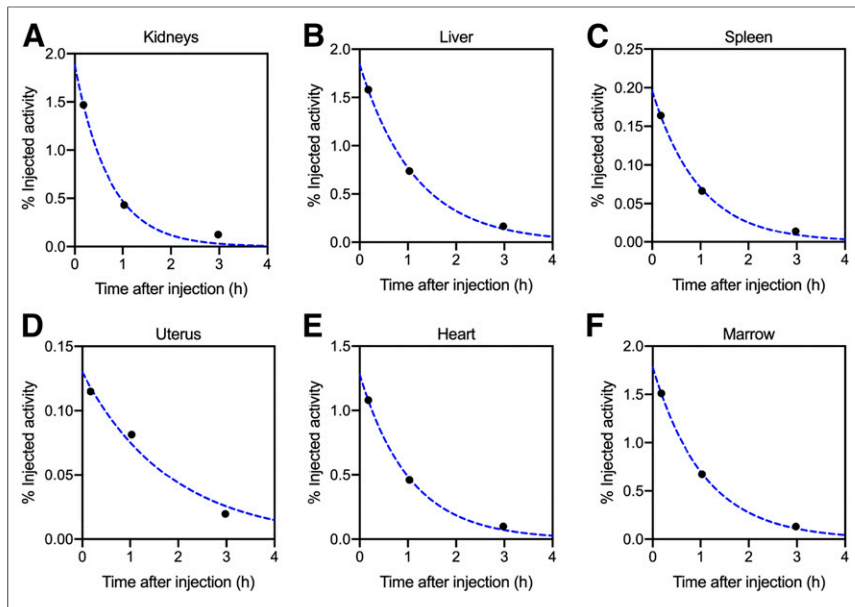| Patient no.	Sex	Age (y)	Diagnosis	Injected activity (MBq)
1	F	63	Cholangiocellular carcinoma	246
2	M	81	Pancreatic cancer with peritonitis carcinomatosa	240
3	F	78	Breast cancer	234
4	M	56	Oropharynx carcinoma	239
5	M	78	Head and neck cancer	214
6	M	62	Gastric cancer	243

FIGURE 2. Percentage injected activity curves for patient 3 are shown for various source organs. Solid circles are measured values, and dotted lines are monoexponential functions fit to data.

Patient-specific masses were used for the liver, kidneys, spleen, uterus, and total body. The organ and total-body/remainder activity kinetic data were then fitted with a monoexponential decay function using OLINDA/EXM. Representative percentage injected activity curves for various source organs for 1 patient are shown in Figure 2. The functions are integrated to obtain time-integrated activity coefficients, and S values are applied

according to MIRD methodology from standard adult phantoms to yield absorbed and effective radiation doses. Radiation weighting factors from International Commission on Radiological Protection publication 60 were applied for calculation of effective doses (26). The calculated doses based on individual patient inputs were then reported as mean ± SD to more accurately represent the general population risk associated with this imaging scan.

Biodistribution

In addition to the contoured tumor and source organ volumes drawn for dosimetry, spheric volumes in the gluteal muscle (range, 7–20 cm^3) and blood pool in the ascending aorta (range, 4–5 mL) were created and automatically propagated to later time points for biodistribution analysis. SUV$_{mean}$ and SUV$_{max}$ were generated for all previously contoured organs and spheric muscle and blood volumes of interest to compute TBRs (tumor SUV$_{max}$/organ SUV$_{mean}$).

RESULTS

PET/CT Imaging

The injected activity of ^{68}Ga-FAPI-46 ranged from 214 to 246 MBq (5.8–6.6 mCi) (Table 1). Images were acquired at 12 ± 2.5 min, 1.2 ± 0.3 h, and 3.3 ± 0.3 h after intravenous administration of ^{68}Ga-FAPI-46. The tracer injection was well tolerated without any side effects in all 6 patients. No adverse events were observed during the 3 h after injection. Maximum-intensity projections and organ volumes used for activity quantification are shown for patient 3 (female) and patient 5 (male) in Figures 3 and 4, respectively. The other patients' images and SUV kinetics are available in supplemental Figures 1–4 (supplemental materials are available at http://jnm.snmjournals.org).
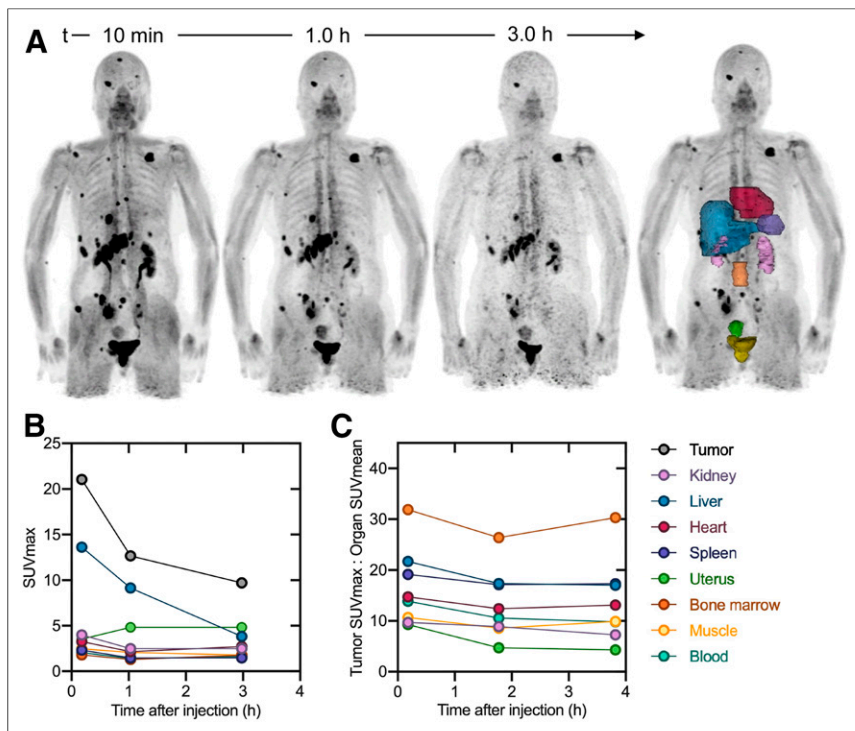
Radiation Dosimetry

The monoexponential curve-fitting parameters and time-integrated activity coefficients (residence times) for each source organ are summarized in Table 2. The pooled patient dosimetry reports from OLINDA/EXM are shown in Table 3.

The organ with the highest absorbed dose was the urinary bladder wall, with 4.83E−02 mGy/MBq, followed by the kidneys (1.60E−02 mGy/MBq), the heart wall (1.11E−02 mGy/MBq), the liver (1.01E−02 mGy/MBq), and the uterus (9.54E−03 mGy/MBq). The remaining organ-absorbed doses were all below 6.96E−03 mGy/MBq. Organs with the highest effective doses were the bladder wall (2.41E−03 mSv/MBq), followed by the ovaries (1.15E−03 mSv/MBq) and red marrow (8.49E−04 mSv/MBq). The average total-body absorbed dose was 5.82E−03 mGy/MBq, and the effective dose was 7.80E−03 mSv/MBq—similar to,

FIGURE 3. Patient 3 (female). (A) ^{68}Ga-FAPI-46 maximum-intensity projections and delineated organs for dose calculations. (B) SUV$_{max}$ at 3 time points after tracer injection. (C) TBR at 3 time points after tracer injection. SUV$_{max}$ and TBR for bladder are excluded from plot. Data values are available in Supplemental Table 1.
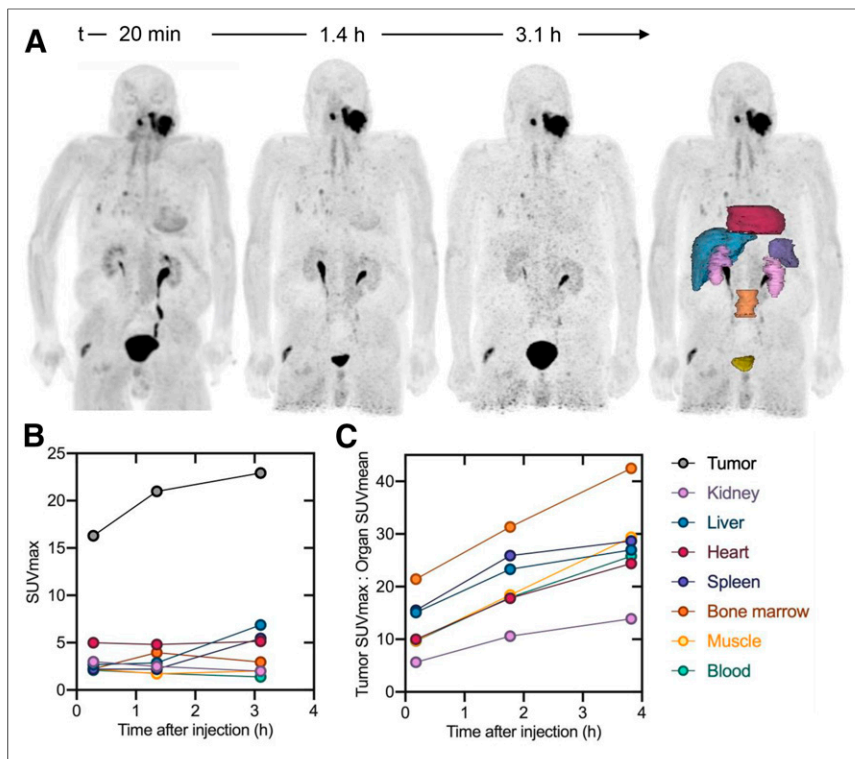
FIGURE 4. Patient 5 (male). (A) ^{68}Ga-FAPI-46 maximum-intensity projection and delineated organs for dose calculations. (B) SUV$_{max}$ at 3 time points after tracer injection. (C) TBR at 3 time points after tracer injection. SUV$_{max}$ and TBR for bladder are excluded from plot. Data values are available in Supplemental Table 1.

though lower than, the reported values for related FAPIs (*21*). Thus, for administration of 200 MBq (5.4 mCi) of ^{68}Ga-FAPI-46, the total-body effective dose was 1.56 ± 0.26 mSv. Together with approximately 3.7 mSv from 1 low-dose CT attenuation scan (*27*), this results in an estimated total effective dose of 5.3 mSv. The reported SDs

TABLE 2
Monoexponential Function Fitting Parameters and Time-Integrated Activity Coefficients (Residence Times) for ^{68}Ga-FAPI-46 in Various Organs

Organ	*A* (%IA)	λ (h^{-1})	TIAC (h)
Liver	3.49 (2.26)	0.88 (0.12)	0.0378 (0.0198)
Kidney	2.07 (0.65)	1.08 (0.26)	0.0195 (0.0062)
Bladder	6.82 (2.32)	1.47 (0.91)	0.0595 (0.0319)
Heart	1.69 (0.30)	0.94 (0.06)	0.0182 (0.0035)
Spleen	0.71 (0.62)	0.96 (0.12)	0.0074 (0.0066)
Marrow	2.61 (0.63)	2.05 (2.97)	0.0250 (0.0114)
Uterus (*n* = 2)	0.13 (0.004)	0.50 (0.07)	0.0027 (0.0005)

A = activity, expressed as %IA = percentage injected activity; %IA = $A \times \exp(-\lambda t)$; λ = rate constant; TIAC = time-integrated activity coefficient.

Data are mean followed by SD in parentheses for 6 patients. Representative percentage injected activity curves with monoexponential curve fits overlaid are available in Supplemental Figure 1. Per-patient coefficients and TIACs are available in Supplemental Table 2.

arise from calculating the mean OLINDA/EXM dosimetry profile from 6 patients and do not account for any possible errors involved in organ delineation.

Biodistribution

Biodistribution data assessed by SUV kinetics for patients 3 (female) and 5 (male) are shown in Figures 3 and 4, respectively. Pooled SUV$_{max}$ and TBR for all 6 patients are summarized in Figure 5; SUV$_{mean}$ is listed in Table 4. The highest average normal-organ SUV$_{max}$ at all time points was observed in the liver, decreasing from an average SUV$_{max}$ of 7.4 at 10 min to 5.0 by 3.3 h (decline of 32%). Tracer uptake in the tumor was rapid, with greater retention than in normal organs: an average SUV$_{max}$ of 15.5 at 10 min and 13.4 at 3.3 h (decrease of 14%).

Tumor and organ mean SUVs decreased in all patients from the first to last time points, whereas TBRs increased with time (with the exception of the uterus TBR). The highest TBR at all time points was observed in the marrow, with a ratio of 31 at 3.3 h. The tumor-to-muscle ratio of 10.7 at 10 min increased more than 2-fold at 3.3 h to 22.8. At 3.3 h, the next highest TBRs were observed in the heart (19.1), spleen (18.9), and liver (16.8).

In summary, the tracer rapidly accumulated in the primary tumors and metastases, with high SUV$_{max}$ and low tracer uptake in normal tissue. The radioactivity was cleared steadily from the blood pool and was excreted via the kidneys, producing high-contrast images.

DISCUSSION

Herein we describe the biodistribution of ^{68}Ga-FAPI-46 and its estimated radiation dose deposition in the organs of 6 cancer patients who underwent ^{68}Ga-FAPI-46 PET/CT imaging at 3 time points. These data are required for clinical translation and approval by regulatory agencies. The average effective whole-body dose for administration of 200 MBq of ^{68}Ga was 1.56 ± 0.26 mSv (7.80E−03 ± 1.31E−03 mSv/MBq). This estimate is slightly lower than the prior reported effective total-body effective doses of other ^{68}Ga-FAPI PET tracers: 1.80E−02 and 1.64E−02 mSv/MBq with ^{68}Ga-FAPI-02 and ^{68}Ga-FAPI-04, respectively (*21*). As a comparison, the reported effective dose for ^{68}Ga-PSMA-11 ranges from 1.08E−02 to 2.46E−02 mSv/MBq (*28,29*), whereas the effective total-body dose of both ^{68}Ga-DOTATOC and ^{68}Ga-DOTATATE is 2.10E−02 ± 3.00E−03 mSv/MBq (*30*).

Despite collection of patient-specific time–activity curves, the dose calculation was based on the stylized phantoms provided in OLINDA/EXM. These estimates provide generalizable population mean absorbed dose values to organs by means of standard phantoms with selected customized organ masses. The reported SD for the dosimetry estimates (Table 3) arise from taking the average of 6 sets of OLINDA/EXM patient reports. There are, however, sources of uncertainty not included in the analysis that are inherent in

TABLE 3
^{68}Ga-FAPI-46 Dosimetry Summary of Mean Absorbed and Effective Doses Using OLINDA/EXM

Organ	Dose per injected activity (mGy/MBq)	Effective dose per injected activity (mSv/MBq)
Adrenals	5.60E−03 (8.12E−04)	2.80E−05 (4.04E−06)
Brain	4.59E−03 (6.12E−04)	2.29E−05 (3.06E−06)
Breasts	4.55E−03 (6.47E−04)	2.28E−04 (3.23E−05)
Gallbladder wall	5.62E−03 (8.53E−04)	—
Lower large intestine wall	5.72E−03 (6.96E−04)	6.86E−04 (8.33E−05)
Small intestine	5.48E−03 (6.37E−04)	2.74E−05 (3.20E−06)
Stomach wall	5.32E−03 (7.25E−04)	6.38E−04 (8.69E−05)
Upper large intestine wall	5.47E−03 (6.97E−04)	2.74E−05 (3.50E−06)
Heart wall	1.11E−02 (1.26E−03)	—
Kidneys	1.60E−02 (4.60E−03)	7.98E−05 (2.29E−05)
Liver	1.01E−02 (7.96E−03)	5.05E−04 (4.00E−04)
Lungs	5.02E−03 (7.09E−04)	6.02E−04 (8.48E−05)
Muscle	4.96E−03 (6.54E−04)	2.48E−05 (3.27E−06)
Ovaries	5.76E−03 (6.91E−04)	1.15E−03 (1.38E−04)
Pancreas	5.69E−03 (8.49E−04)	2.84E−05 (4.24E−06)
Red marrow	7.08E−03 (1.00E−03)	8.49E−04 (1.20E−04)
Osteogenic cells	9.38E−03 (1.30E−03)	9.38E−05 (1.30E−05)
Skin	4.41E−03 (6.33E−04)	4.41E−05 (6.33E−06)
Spleen	6.96E−03 (2.76E−03)	3.48E−05 (1.39E−05)
Testes	4.88E−03 (6.69E−04)	1.15E−03 (1.38E−04)
Thymus	5.10E−03 (6.40E−04)	2.55E−05 (3.21E−06)
Thyroid	4.84E−03 (5.72E−04)	2.42E−04 (2.85E−05)
Urinary bladder wall	4.83E−02 (8.55E−03)	2.41E−03 (4.27E−04)
Uterus	9.54E−03 (5.36E−03)	4.76E−05 (2.67E−05)
Total body	5.82E−03 (1.18E−03)	7.80E−03 (1.31E−03)
Total body dose for 200 MBq	1.16 mGy (0.24 mGy)	1.56 mSv (0.26 mSv)

Data are mean followed by SD in parentheses for 6 patients. Effective doses in ovaries and testes are equivalent because of use of hermaphroditic adult phantom weighting. Gallbladder wall and heart wall effective doses are not available based on ICRP radiation weighting factors. Nonpooled OLINDA/EXM reports, including β and photon contribution to total dose, are available in Supplemental Table 3.

the dose calculation process and propagate to the final dose result. One of the most significant contributing sources of uncertainty is the organ volume delineation itself (*31,32*). Interpatient variability is also seen within Table 2, which shows a relatively high SD for time–activity curve-fitting parameters, most prominently observed in the liver.

Although tumor dosimetry was not addressed directly in this study, the trend in biodistribution observed up to 3.3 h after tracer administration demonstrates rapid tumor uptake and satisfactory retention. FAPI-46 biodistribution and dosimetry (including tumor dosimetry) using longer-lived isotopes for therapeutic applications remain to be studied. Such studies are essential to evaluate longer-term tracer kinetics and thereby determine rational therapeutic isotope conjugates with a well-matched physical half-life. The promising trend observed thus far of increasing TBRs over time seems to be favorable for therapeutic applications. Given the high achieved TBRs even at 10 min, early-time-point imaging with ^{68}Ga-FAPI becomes possible; however, it should be considered that the contrast ratio improves with time.
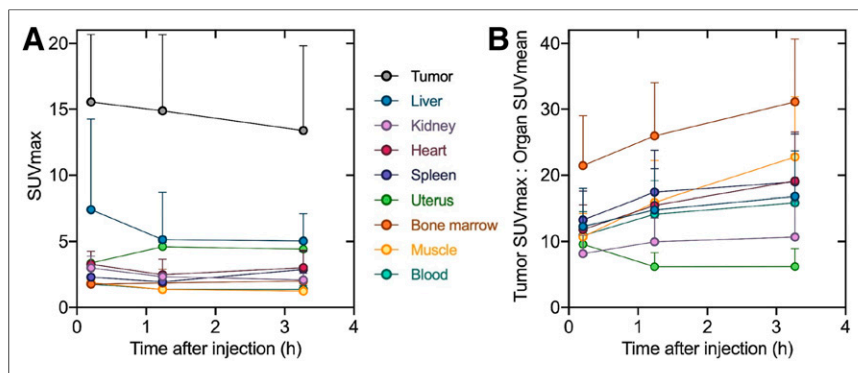
FIGURE 5. Pooled tumor and organ SUV$_{max}$ (A) and TBR (B) at 3 time points after tracer injection (excluding bladder). Results are shown as mean and SD for 6 patients. Data values are available in Table 4.

TABLE 4
Pooled Tumor-to-Organ SUV Ratio, SUV_{max}, and SUV_{mean} at 3 Time Points After ^{68}Ga-FAPI-46 Administration

Parameter	10 min	1.2 h	3.3 h
SUV_{max}-to-SUV_{mean} ratio			
Tumor-to-liver	12.28 (5.75)	14.79 (6.22)	16.80 (6.90)
Tumor-to-kidney	8.17 (2.76)	9.96 (3.64)	10.68 (5.34)
Tumor-to-blood	10.89 (3.61)	14.15 (5.02)	15.87 (7.30)
Tumor-to-muscle	10.71 (3.56)	15.91 (6.33)	22.77 (9.15)
Tumor-to-heart	11.78 (3.76)	15.48 (5.49)	19.11 (7.44)
Tumor-to-spleen	13.27 (4.31)	17.44 (6.36)	18.99 (7.27)
Tumor-to-marrow	21.46 (7.56)	25.96 (8.09)	31.13 (9.52)
Tumor-to-uterus ($n = 2$)	9.60 (0.46)	6.19 (2.12)	6.20 (2.70)
SUV_{max}			
Tumor	15.54 (5.13)	14.89 (5.77)	13.39 (6.44)
Liver	7.42 (6.84)	5.15 (3.56)	5.04 (2.07)
Kidney	3.00 (0.89)	2.33 (0.26)	2.08 (0.49)
Blood	1.77 (0.35)	1.38 (0.26)	1.37 (0.31)
Muscle	1.87 (0.49)	1.37 (0.45)	1.24 (0.56)
Heart	3.28 (1.00)	2.48 (1.17)	3.02 (1.31)
Spleen	2.30 (0.23)	1.94 (0.42)	2.88 (1.38)
Marrow	1.77 (0.34)	1.85 (1.05)	2.00 (0.59)
Uterus ($n = 2$)	3.37 (0.23)	4.61 (0.32)	4.42 (0.58)
SUV_{mean}			
Tumor	3.87 (1.30)	3.37 (1.11)	2.81 (1.44)
Liver	1.51 (0.96)	1.10 (0.58)	0.81 (0.34)
Kidney	1.92 (0.34)	1.47 (0.17)	1.25 (0.22)
Blood	1.43 (0.25)	1.03 (0.15)	0.83 (0.15)
Muscle	1.48 (0.41)	0.96 (0.32)	0.61 (0.24)
Heart	1.32 (0.21)	0.95 (0.15)	0.68 (0.15)
Spleen	1.17 (0.20)	0.85 (0.17)	0.69 (0.16)
Marrow	0.73 (0.12)	0.56 (0.11)	0.41 (0.10)
Uterus ($n = 2$)	2.08 (0.27)	2.53 (0.24)	1.97 (0.42)

Data are mean followed by SD in parentheses for 6 patients.

This analysis was limited to 6 cancer patients (4 men and 2 women) and no healthy subjects. The basal FAP expression profile of a greater variety of cancers, as well as in healthy subjects, remains to be quantitatively assessed. It is, however, known that FAP is expressed at sites of arthritis, wound healing and active tissue remodeling, bone marrow mesenchymal cells, and cirrhotic liver (5,18,33,34). The extent of this expression and its impact on imaging and potential therapies require further clinical study. Implementation of FAP-targeted therapies thereby necessitates a better understanding of the comprehensive role of FAP, not only in the tumor microenvironment and carcinogenesis of different cancer types but also in widespread bodily fibrotic mechanisms. Evaluation of ^{68}Ga-FAPI-46 diagnostic accuracy was outside the study scope.

CONCLUSION

^{68}Ga-FAPI-46 PET/CT imaging is shown to have a favorable dosimetry profile. For administration of 200 MBq (5.4 mCi) of ^{68}Ga-FAPI-46, the effective whole-body dose of a PET scan is 1.56 ± 0.26 mSv. When including a low-dose CT scan (3.7 mSv), the dose of a ^{68}Ga-FAPI-46 PET/CT scan is approximately 5.3 mSv in total. The biodistribution study showed high TBRs increasing over time, suggesting high diagnostic performance and favorable tracer kinetics for potential therapeutic applications. Long-term tracer biodistribution and dosimetry for longer-lived therapeutic isotope applications remain to be studied. Further work is needed to better identify indications for FAPI PET/CT and its diagnostic accuracy.

DISCLOSURE

licensed to Sofie Biosciences and Trethera Therapeutics. This intellectual property was not used in the current study. Sebastien Vauclin is an employee of DOSIsoft SA (Cachan, France). Uwe Haberkorn and Thomas Lindner are coauthors on a patent application for FAP agents. No other potential conflict of interest relevant to this article was reported.

KEY POINTS

QUESTION: What is the biodistribution and radiation dosimetry profile of 68Ga-FAPI-46, a new PET tracer targeting tumor stroma with high potential for theranostic applications?

PERTINENT FINDINGS: Based on 3 serial 68Ga-FAPI-46 PET/CT scans acquired in 6 cancer patients, the average effective whole-body dose estimation for administration of 200 MBq of 68Ga-FAPi-46 was 1.56 mSv, which is lower than with other 68Ga PET tracers (68Ga-PSMA-11 or 68Ga-DOTATATE). The biodistribution study showed high TBRs increasing over time.

IMPLICATIONS FOR PATIENT CARE: This study confirms the high potential of 68Ga-FAPI-46 for theranostic applications and provides required data for translation and approval by regulatory agencies.

REFERENCES

1. Chen X, Song E. Turning foes to friends: targeting cancer-associated fibroblasts. *Nat Rev Drug Discov.* 2019;18:99–115.
2. Katayama Y, Uchino J, Chihara Y, et al. Tumor neovascularization and developments in therapeutics. *Cancers (Basel).* 2019;11:E316.
3. Weis SM, Cheresh DA. Tumor angiogenesis: molecular pathways and therapeutic targets. *Nat Med.* 2011;17:1359–1370.
4. Puré E, Blomberg R. Pro-tumorigenic roles of fibroblast activation protein in cancer: back to the basics. *Oncogene.* 2018;37:4343–4357.
5. Brennen WN, Isaacs JT, Denmeade SR. Rationale behind targeting fibroblast activation protein-expressing carcinoma-associated fibroblasts as a novel chemotherapeutic strategy. *Mol Cancer Ther.* 2012;11:257–266.
6. Garin-Chesa P, Old LJ, Rettig WJ. Cell surface glycoprotein of reactive stromal fibroblasts as a potential antibody target in human epithelial cancers. *Proc Natl Acad Sci USA.* 1990;87:7235–7239.
7. Shiga K, Hara M, Nagasaki T, Sato T, Takahashi H, Takeyama H. Cancer-associated fibroblasts: their characteristics and their roles in tumor growth. *Cancers (Basel).* 2015;7:2443–2458.
8. Lo A, Li CP, Buza EL, et al. Fibroblast activation protein augments progression and metastasis of pancreatic ductal adenocarcinoma. *JCI Insight.* 2017;2:e92232.
9. Gao LM, Wang F, Zheng Y, Fu ZZ, Zheng L, Chen LL. Roles of fibroblast activation protein and hepatocyte growth factor expressions in angiogenesis and metastasis of gastric cancer. *Pathol Oncol Res.* 2019;25:369–376.
10. Liu J, Huang C, Peng C, et al. Stromal fibroblast activation protein alpha promotes gastric cancer progression via epithelial-mesenchymal transition through Wnt/beta-catenin pathway. *BMC Cancer.* 2018;18:1099.
11. Jia J, Martin TA, Ye L, et al. Fibroblast activation protein-alpha promotes the growth and migration of lung cancer cells via the PI3K and sonic hedgehog pathways. *Int J Mol Med.* 2018;41:275–283.
12. Zi FM, He JS, Li Y, et al. Fibroblast activation protein protects bortezomib-induced apoptosis in multiple myeloma cells through beta-catenin signaling pathway. *Cancer Biol Ther.* 2014;15:1413–1422.
13. Zi F, He J, He D, Li Y, Yang L, Cai Z. Fibroblast activation protein alpha in tumor microenvironment: recent progression and implications (review). *Mol Med Rep.* 2015;11:3203–3211.
14. Liu F, Qi L, Liu B, et al. Fibroblast activation protein overexpression and clinical implications in solid tumors: a meta-analysis. *PLoS One.* 2015;10:e0116683.
15. Lindner T, Loktev A, Altmann A, et al. Development of quinoline-based theranostic ligands for the targeting of fibroblast activation protein. *J Nucl Med.* 2018;59:1415–1422.
16. Loktev A, Lindner T, Mier W, et al. A tumor-imaging method targeting cancer-associated fibroblasts. *J Nucl Med.* 2018;59:1423–1429.
17. Loktev A, Lindner T, Burger EM, et al. Development of novel FAP-targeted radiotracers with improved tumor retention. *J Nucl Med.* 2019;60:1421–1429.
18. Kratochwil C, Flechsig P, Lindner T, et al. 68Ga-FAPI PET/CT: tracer uptake in 28 different kinds of cancer. *J Nucl Med.* 2019;60:801–805.
19. Röhrich M, Loktev A, Wefers AK, et al. IDH-wildtype glioblastomas and grade III/IV IDH-mutant gliomas show elevated tracer uptake in fibroblast activation protein-specific PET/CT. *Eur J Nucl Med Mol Imaging.* 2019;46:2569–2580.
20. Giesel FL, Heussel CP, Lindner T, et al. FAPI-PET/CT improves staging in a lung cancer patient with cerebral metastasis. *Eur J Nucl Med Mol Imaging.* 2019;46:1754–1755.
21. Giesel FL, Kratochwil C, Lindner T, et al. 68Ga-FAPI PET/CT: biodistribution and preliminary dosimetry estimate of 2 DOTA-containing FAP-targeting agents in patients with various cancers. *J Nucl Med.* 2019;60:386–392.
22. Hamson EJ, Keane FM, Tholen S, Schilling O, Gorrell MD. Understanding fibroblast activation protein (FAP): substrates, activities, expression and targeting for cancer therapy. *Proteomics Clin Appl.* 2014;8:454–463.
23. Loevinger R, Budinger TF, Watson EE. *MIRD Primer for Absorbed Dose Calculations.* Reston, VA: Society of Nuclear Medicine and Molecular Imaging; 1991:1–17.
24. Bolch WE, Eckerman KF, Sgouros G, Thomas SR. MIRD pamphlet no. 21: a generalized schema for radiopharmaceutical dosimetry—standardization of nomenclature. *J Nucl Med.* 2009;50:477–484.
25. Hindorf C, Glatting G, Chiesa C, Linden O, Flux G. EANM Dosimetry Committee guidelines for bone marrow and whole-body dosimetry. *Eur J Nucl Med Mol Imaging.* 2010;37:1238–1250.
26. ICRP. 1990 recommendations of the International Commission on Radiological Protection: ICRP Publication 60. *Ann ICRP.* 1991;21:1–201.
27. Huang B, Law MW, Khong PL. Whole-body PET/CT scanning: estimation of radiation dose and cancer risk. *Radiology.* 2009;251:166–174.
28. Afshar-Oromieh A, Hetzheim H, Kubler W, et al. Radiation dosimetry of 68Ga-PSMA-11 (HBED-CC) and preliminary evaluation of optimal imaging timing. *Eur J Nucl Med Mol Imaging.* 2016;43:1611–1620.
29. Pfob CH, Ziegler S, Graner FP, et al. Biodistribution and radiation dosimetry of 68Ga-PSMA HBED CC: a PSMA specific probe for PET imaging of prostate cancer. *Eur J Nucl Med Mol Imaging.* 2016;43:1962–1970.
30. Sandström M, Velikyan I, Garske-Roman U, et al. Comparative biodistribution and radiation dosimetry of 68Ga-DOTATOC and 68Ga-DOTATATE in patients with neuroendocrine tumors. *J Nucl Med.* 2013;54:1755–1759.
31. Lassmann M, Eberlein U. The relevance of dosimetry in precision medicine. *J Nucl Med.* 2018;59:1494–1499.
32. Gear JI, Cox MG, Gustafsson J, et al. EANM practical guidance on uncertainty analysis for molecular radiotherapy absorbed dose calculations. *Eur J Nucl Med Mol Imaging.* 2018;45:2456–2474.
33. Keane FM, Yao TW, Seelk S, et al. Quantitation of fibroblast activation protein (FAP)-specific protease activity in mouse, baboon and human fluids and organs. *FEBS Open Bio.* 2013;4:43–54.
34. Yazbeck R, Jaenisch SE, Abbott CA. Potential disease biomarkers: dipeptidyl peptidase 4 and fibroblast activation protein. *Protoplasma.* 2018;255:375–386.